RESEARCH ARTICLE

On the flow conditions requiring detailed geometric modeling for multiscale evaluation of coastal forests

Reika Nomura[1*] , Shinsuke Takase[2], Shuji Moriguchi[1] and Kenjiro Terada[1]

*Correspondence:
nomura@irides.tohoku.ac.jp
International Research Institute
of Disaster Science (IRIDeS),
Tohoku University, Sendai, Japan
Department of Civil Engineering
and Architecture, Hachinohe
Institute of Technology,
Hachinohe, Japan

Abstract

The multiscale evaluation method is applied to assess the influence of detailed geometric modeling of trees on their macroscopic attenuation effect against tsunami-like flow. Specifically, we conduct a series of numerical flow tests (NFTs), i.e., 3D flow simulations in a local test domain (LTD), under various inflow conditions to evaluate the macroscopic flow characteristics in the LTD accommodating an array of either simple cylinder or detailed tree models that mimic a coastal forest. After the procedure of NFTs in the multiscale evaluation method is briefly summarized and the corresponding governing equations and analysis conditions are presented, we introduce two indices for evaluating the macroscopic flow characteristics within the framework of multiscale modeling. Based on the NFT results, we discuss how the modeling scheme for trees influences the macroscopic flow characteristics in terms of these indices and clarify the microscopic mechanisms that influence the macroscopic attenuation property. Additionally, the NFT results are compared with the experimental results to justify these discussions, and key factors are explored in terms of reproducing real phenomena. In addition, to apply the multiscale evaluation method to assess the disaster mitigation performance of various types of ecosystems in a realistic situation, we discuss under what circumstances and with what level of detail vegetation should be modeled.

Keywords: Multiscale evaluation, Numerical flow test, Coastal forests, Attenuation effects, Geometric modeling of trees, Tsunami mitigation

Introduction

As global awareness of disaster mitigation is growing, the scientific community has taken an interest in the concept of ecosystem-based disaster risk reduction (Eco-DRR), a strategy realized by maintaining ecosystems such as forests, wetlands, and coral reefs. These ecosystems are expected to "act as natural infrastructure, reducing physical exposure to various hazards" [1]. Accordingly, Eco-DRR is mentioned several times in the Sendai Framework for Disaster Risk Reduction 2015–2030 [2], indicating that the utilization of natural resources for disaster mitigation purposes is being recognized worldwide. Among all different types of Eco-DRR systems, forests are representative and have thus attracted

Nomura *et al. Advanced Modeling and Simulation in Engineering Sciences*(2023)10:13

Page 2 of 25

considerable attention. Shuto [3] was the first to perform fundamental investigations of the performance of natural trees for mitigating water-related hazards. Following his pioneering work, many observational studies have demonstrated the potential of natural trees for reducing the risks of natural disasters [4–6]. Indeed, as a result of the lessons learned from the Great East Japan Earthquake and the resulting tsunamis, coastal forest is presently considered a component of multiple defense systems to protect against tsunamis [7–9].

To further promote coastal forest as a sustainable and effective disaster mitigation system, a substantial number of studies have been conducted to understand the performance of natural trees. Conventional numerical and experimental studies have used a group of vertical columns that mimic a natural forest, e.g., [10–15]. For example, on the basis of numerical simulations on an array of cylinders, Maza et al. [15] emphasized the relative importance of the overall tree density over the domain. Anjum and Tanaka [16] experimentally investigated flow through vegetation modeled by a combination of tall/short circular cylinders and clarified the resultant energy dissipation due to the discontinuous vertical distribution of cylinders. In addition, some researchers have tried to reflect the complex morphology of trees in inundation simulations; see, e.g., [17–21] with a view to practical applications. However, most of these models are limited to two-dimensional (2D) expressions; hence, the effect of complex geometries has not been sufficiently considered thus far.

To fully evaluate the performance of complex tree geometries, 3D tree models are considered to be essential. For instance, the complex root system of mangrove trees has been confirmed to dramatically improve the flow attenuation property; thus, to better estimate the flow through mangrove stands, mangrove trees have been modeled in three dimensions [22–25]. Furthermore, Maza et al. [20] conducted hydraulic experiments on 3D-printed tree models and reported that the flow speed inside a complex vegetation geometry is up to 50% lower than that in other zones. Such 3D tree modeling is feasible based on recent 3D scanning techniques and plant modeling algorithms [26–29]. Nevertheless, 3D numerical simulation of flow through a group of trees with complex geometry is computationally intensive and therefore requires an efficient approach.

According to demands on the 3D modeling of trees with reasonable computational cost, we originally presented a multiscale evaluation method for determining their drag effects [30]. In that method, by employing a flow simulation scheme for the Navier–Stokes equations, we conduct "numerical flow tests" (NFTs) for the "local test domain" (LTD), a sort of representative elementary volume (REV) [31], in which a limited number of trees are regularly placed to capture the geometrical features of trees. Then, homogenization or spatial averaging is carried out to characterize the "macroscopic" attenuation property that reflects the "microscopic" mechanisms of flow through a coastal forest. Since the effectiveness and capability of the proposed method were well demonstrated in a previous study [30], we can now make further arguments against tree modeling. That is, we are ready to answer the following question: in what situation do we need to model the coastal forest by an array of trees with complex tree geometries instead of simple vertical cylinders, or vice versa?

To answer the question posed above, in this paper, we investigate the flow conditions requiring detailed geometric modeling for multiscale evaluation of coastal forests In other words, along the lines of the previous multiscale evaluations [30], we try to reveal the specific flow situations in the 2D macroscopic simulations to highlight the significant

contradictions between the actual performance of coastal forests and the estimated ones due to insufficiency of geometric tree modeling. For this purpose, we trace the numerical flow tests, i.e., 3D flow simulations in the LTD introduced in the previous study, and then calculate the macroscopic flow attenuation as the spatial and temporal averaging values for the microscopic flow mechanics around a tree's geometry. Specifically, by arranging simple cylinder and detailed tree models in an open channel that mimics a coastal forest, we conduct a series of NFTs under various inflow conditions with different inflow velocities and depths and discuss the effect of the canopies of the tree model from the comparison between two models. After the procedure of NFTs along the lines of the multiscale evaluation method is briefly summarized and the corresponding governing equations and analysis conditions are presented, we introduce two indices for evaluating the macroscopic flow attenuation characteristics. Then, the NFT results are investigated from the macro- and microscopic perspectives; that is, we discuss how the geometry modeling for trees influences the macroscopic flow characteristics in terms of these indices and clarify the microscopic mechanisms that influence the macroscopic attenuation property. Additionally, the NFT results are compared with the experimental results to justify these discussions, and key factors are explored in terms of reproducing real phenomena. In addition, to apply the multiscale evaluation method to assess the disaster mitigation performance of various types of ecosystems in realistic situations, we discuss under what circumstances and with what level of detail vegetation should be modeled.

A preliminary study was conducted by performing NFTs on isolated canopied-tree and cylinder models at various combinations of inflow depths and velocities, and the results are presented in Appendix A, from which the validity of 3D flow simulations in this study is confirmed. For 3D flow simulations in the LTD necessary for the NFTs, we employ the stabilized finite element method (FEM) [32,33] incorporated with the phase-field method [34,35]. It is worth mentioning that this study does not demonstrate the 2D macroscopic flow simulations, although the 3D microscopic flow simulations are regarded as NFTs in the previous multiscale modeling. Thus, the aim of this study is limited to quantitatively arguing the necessity of advanced modeling in the 3D NFTs, though the supposed achievements are expected to eventually contribute to the performance evaluation of the coastal forests.

Numerical flow tests for identifying flow conditions requiring detailed geometric modeling

Multiscale evaluation of coastal forests

This section is devoted to describing the multiscale evaluation method for assessing the disaster mitigation performance of trees that was recently proposed in our previous work [30].

In the context of multiscale modeling, we assume that the macroscopic flow characteristics (Fig. 1a) can be evaluated by performing the spatial averaging of the flow characteristics in a representative domain on the local or, equivalently, microscopic scale, which is illustrated in Fig. 1b. In other words, the method proposed in the previous study [30] hinges on NFTs to be conducted in the "local test domain (LTD)" that contains arrays of the detailed tree or circular cylinder models. The idea of NFTs with an LTD underlies the theory of spatial averaging based on the scale separation principle as commonly assumed in computational homogenization; see [36–38].
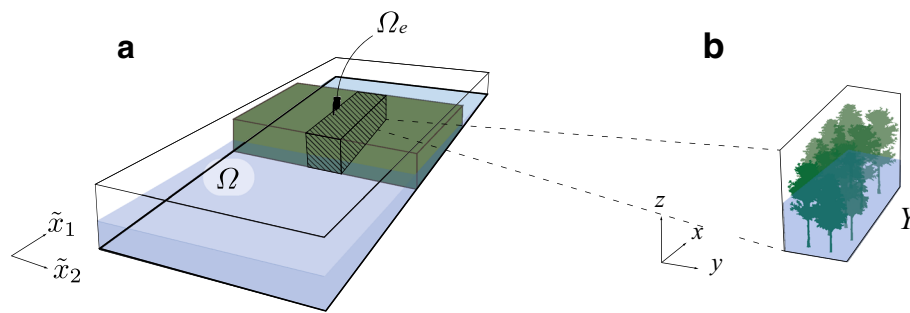
Fig. 1 Concept of spatial-scale separation: **a** macroscopic flow, where the results of numerical flow tests are finally reflected, and (**b**) local test domain (LTD), which is assumed to be a representative elementary volume (REV) for our numerical flow tests. See Nomura et al. [30] for a more detailed explanation of spatial-scale separation

Here, the macroscopic flows in Fig. 1a are supposed to be simulated by the 2D equations (e.g., shallow water equation) for computational efficiency, while the 3D Navier–Stokes equations are to be employed for the local scale simulation. Needless to say, since the macroscopic flow simulations are significantly affected by how to achieve the local test domain (LTD) illustrated in Fig. 1b. The NFT scheme, its resolution scale, or the LTD size have nonnegligible influences on the ultimate results of the evaluated macroscopic property. Nevertheless, expressing the effects of tree geometry should be the primary topic for such arguments. To clarify this point, we focus on the process of 3D NFTs, especially for the LTD setup, as mentioned in the first section.

In what follows, the established LTD, accommodating either tree models with detailed geometry or simple cylinders, is first explained. Second, we present the equations governing the motion of 3D local flow inside the LTD along with the boundary/initial conditions used for NFTs. Analysis conditions for the finite element (FE) flow simulation are also provided. Finally, to investigate the effects of modeling trees in detail, we introduce two indices to evaluate the macroscopic attenuation effect.

Tree model with canopy and circular cylinder model

As mentioned in the Introduction, we set up two types of tree models: a model with a canopy that imitates the fairly detailed geometry of an actual tree and a circular cylinder model. Hereafter, the former and latter are simply referred to as the "canopied-tree model" and "cylinder model", respectively. Both models are arrayed in a rectangular open channel, which is employed as the LTD. Each array inside the LTD consists of 26 structures (either canopied-tree or cylinder models) located at an interval of 0.1 [m]. Here, the LTD is a kind of REV according to the theory of flow through porous media [31]. See the previous study [30] for a detailed explanation and a description of the LTD concept. In this study, the rectangular open channel has dimensions of 3.12 m × 0.2 m × 0.5 m (length × width × height) for the LTD.

The canopied-tree model consists of a central trunk and 30 branches, as shown in Fig. 2a, where the canopy is mounted on the upper part of the cylindrical trunk. Six branches are located at the same height, and each branch is inclined 45° with respect to the horizontal floor. While the complex shape is established in the canopied-tree model, the cylinder model has a cylindrical trunk only, as illustrated in Fig. 2b. The heights of both models are the same and set at 0.22 [m], but only the cylindrical trunk parts of both models have the
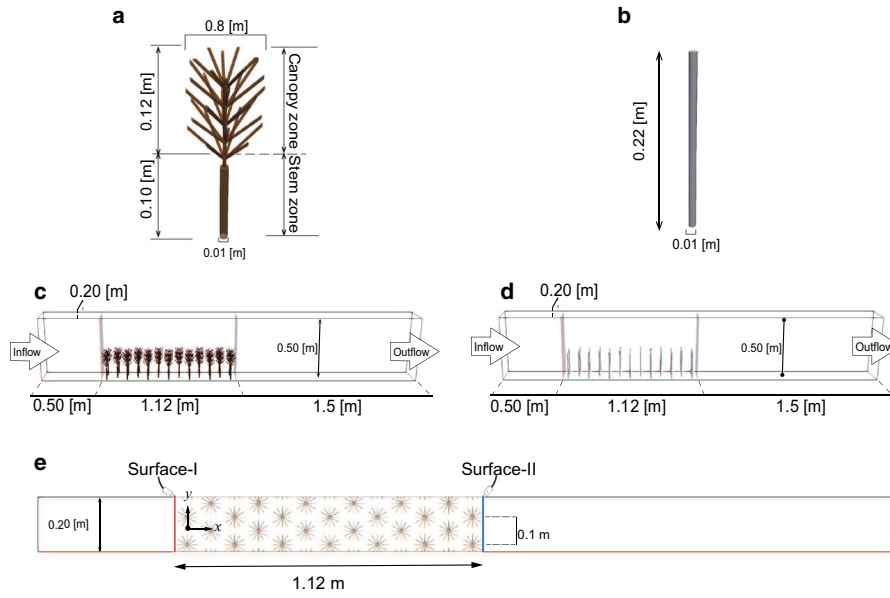
Fig. 2 Setup of numerical flow tests in the LTD accommodating either tree models with a detailed geometry or circular cylinders. **a** Canopied tree model; **b** cylinder model; **c**, **d** rectangular open channel, i.e., LTD with both models; **e** top view of the LTD with the staggered arrangements of 26 tree models

same diameter set at 0.01 [m]. It is, however, noted that both models are treated as rigid (that is, undeformable) bodies in this study. Note that the spatial scale of the LTD in this study is also set to be consistent with the model experiment conducted by Hayashi et al. [39] using miniature trees for validation purposes, in line with the previous setting [30].

Governing equations for NFTs in the LTD

As shown in Fig. 1b, the LTD is denoted by Y and divided into three subdomains as

$$Y = Y_{\mathrm{air}} \cup Y_{\mathrm{f}} \cup Y_{\mathrm{s}}, \tag{1}$$

where Y_{air}, Y_{f}, and Y_{s} are the domains of air, water and the group of vertical structures, respectively. Here, Y_{s} can be further represented as

$$Y_{\mathrm{s}} = \sum_{j=1}^{N} Y_{\mathrm{s},j}, \tag{2}$$

where N denotes the total number of vertical structures inside the LTD, and $Y_{\mathrm{s},j}$ is the domain occupied by the j-th structure. As mentioned above, we set $N = 26$ as in Fig. 2e in this study. Since each vertical structure is assumed to be rigid, a boundary of $Y_{\mathrm{s},j}$ is considered a spatially fixed surface against the flow.

We employ the following 3D Navier–Stokes equations to simulate the flow through an array of either the canopied-tree or cylinder models:

$$\left. \begin{aligned} \rho \left(\frac{\partial \boldsymbol{u}}{\partial t} + \boldsymbol{u} \cdot \nabla \boldsymbol{u} \right) &= \nabla \cdot \boldsymbol{\sigma} + \boldsymbol{b} \\ \nabla \cdot \boldsymbol{u} &= 0 \end{aligned} \right\} \quad \text{in} \quad Y_{\mathrm{air}} \cup Y_{\mathrm{f}}, \tag{3}$$

where $\boldsymbol{u}$ is the flow velocity vector, ρ is the mass density, and $\boldsymbol{b}$ is the body force vector due to gravity. For a Newtonian fluid such as water, the stress tensor $\boldsymbol{\sigma}_{\mathrm{f}}$ is given as

$$\boldsymbol{\sigma} = -P\boldsymbol{I} + 2\mu\boldsymbol{d}, \tag{4}$$

Nomura *et al. Advanced Modeling and Simulation in Engineering Sciences* (2023) 10:13

Page 6 of 25

Table 1 Information about stabilized finite element flow simulations

Model type	Tree	Cylinder
Nodes	6,177,902	1,031,043
Elements	35,313,776	5,341,362
Element size: πd	1:40	
Time step Δt	0.001 [s]	
Data sampling	100 [Hz] (Per 0.01 [s])	
Density ρ	998 [kg/m^3]	
Viscosity μ	1.01e−3 [Pas]	

where P and μ and $\boldsymbol{d}$ denote the pressure, viscosity and the strain rate tensor, respectively.

To discretize Eq. (3), we employ the SUPG/PSPG stabilized FEM [32]. Additionally, the Crank-Nicolson scheme is applied for temporal discretization. Notably, turbulence stresses are not considered in our simulations because they are considered to be much smaller than the drag effects caused by the array of trees or plants, as reported in [40]. The specific numbers of elements and nodes for our FE flow simulations are summarized in Table 1 along with the other parameters. In addition, the phase-field method is utilized to capture the motion of a water free surface; see, for example, Chiu and Lin [34] and Takada et al. [35] for a detailed explanation. Thus, the viscosity μ and the density ρ in the momentum equations are defined by the following simple mixture rules.

$$\rho = \rho_f \cdot \phi + \rho_{air} \cdot (1 - \phi), \tag{5}$$

$$\mu = \mu_f \cdot \phi + \mu_{air} \cdot (1 - \phi), \tag{6}$$

where ϕ is the phase field variable evaluated at each nodal point which determines the interface between Y_f and Y_{air}, so that every point belongs to either the water domain Y_f ($\phi = 1.0$) or the air domain Y_{air} ($\phi = 0.0$). Thus, the boundary surface ∂Y_{free} can be expressed as:

$$\partial Y_{free} = \{\boldsymbol{x} \in Y_f \cup Y_{air} \mid \phi(\boldsymbol{x}) = 0.5\} \tag{7}$$

Additionally, the application of the stabilized FEM to free surface flow simulations is well demonstrated in Takase et al. [41].

Boundary, initial and inflow conditions

The boundary conditions are established on the boundary surface of the flow domain Y_f inside the LTD Y. The boundary domain is denoted by ∂Y and is represented as

$$\partial Y_f = \partial Y_{\pm 1} \cup \partial Y_{\pm 2} \cup \partial Y_s^* \cup \partial Y_{bottom} \cup \partial Y_{free}, \tag{8}$$

where $\partial Y_{\pm i}$ represents the i-th surfaces with signs '$\pm$' indicating the directions of the outward unit normal vectors with respect to the coordinate axes. Here, Y_s^* indicates the domain of the submerged structures, which is the subset of that of whole structures ($Y_s^* \subseteq Y_s$), Y_s, and then its boundary surface is expressed with ∂Y_s^*. Additionally, ∂Y_{bottom} and ∂Y_{free} are the free and bottom surfaces, respectively.

Nonslip conditions are imposed on the bottom surface and the surfaces of the vertical structures as

$$\boldsymbol{u}|_{\partial Y_{bottom} \cup \partial Y_s^*} = \boldsymbol{0}. \tag{9}$$

Additionally, to consider the group or crowd effect for a limited simulation domain in the direction orthogonal to the overall flow, the following periodic boundary condition is employed:

$$\boldsymbol{u}|_{\partial Y_{-2}} = \boldsymbol{u}|_{\partial Y_2}. \tag{10}$$

Inflow $\hat{\boldsymbol{u}}$ is applied on the upwind surface of the LTD as

$$\boldsymbol{u}|_{\partial Y_{-1}} = \hat{\boldsymbol{u}} = \begin{Bmatrix} \hat{u}_1 \\ 0 \\ 0 \end{Bmatrix}, \tag{11}$$

which has the prescribed component $\hat{u}_1$ only in the direction parallel to the overall flow, i.e., the x_1-direction. Note that this setting of boundary conditions is based on the assumption that the scale separation principle is applicable. That is, it is assumed that the LTD is sufficiently small compared to the macroscopic domain and that the macroscopic fields are constant within the local domain while variable at the macroscopic scale. As a result, the periodic boundary condition in the lateral direction is valid for obtaining the macroscopic attenuation property depending on an arbitrary flow velocity and depth, but not intended to directly simulate actual flow phenomena such as tsunamis.

A Sommerfeld nonreflecting boundary condition [42] is applied to the outflow surface ∂Y_{+1} by solving the radiation equation; see Yoshida and Watanabe [43] for a detailed explanation. Additionally, the inflow depth $\hat{h}$ is prescribed to control the flow rate in conjunction with the condition in Eq. (11). When the initial value of $\hat{h}$ is determined on ∂Y_{-1} in the inflow condition, the initial height of the water-air interface in the whole domain is set equal to $\hat{h}$.

Conversion of speed by Froude number

The flow condition around trees at the real scale is associated with that of miniature models using the Froude number as established in our previous study [30]. Specifically, the Froude number of the inflow in our NFTs as well as the model experiment [39] is assumed to be the same as that of the actual scale flow, so that the following condition is satisfied:

$$\text{Fr} = \frac{\hat{u}_1}{\sqrt{gL}} = \frac{\mathcal{U}}{\sqrt{g\mathcal{L}}} \tag{12}$$

where $\hat{u}_1$ and L are the inflow speed and the representative length of the LTD for NFTs, respectively, and $\mathcal{U}$ and $\mathcal{L}$ are the flow speed and the representative length of the structure in a realistic situation, respectively.

When the tree height at the real scale is set to be λ times larger than that of the miniature tree, the flow speed and the representative length in a realistic situation can be written as

$$\mathcal{L} = \lambda L, \tag{13}$$

$$\mathcal{U} = \sqrt{g\mathcal{L}} \cdot \text{Fr} = \lambda^{1/2} \cdot \hat{u}_1. \tag{14}$$

Note that the pressure calculated in our NFT is $1/\lambda$ times smaller than the value exerted on a realistic scale according to this equivalency of the Froude number.

Indices for macroscopic flow characteristics

Two indices are introduced to characterize the macroscopic flow. Based on the theory of multiscale evaluation, we first define the time averaging of time-varying data as

$$\bar{\bullet} = \frac{1}{T} \int_{t-T}^{t} \bullet \; dt, \tag{15}$$

where t is the termination time of a simulation. Additionally, T is the time averaging interval and set to be the period during which to attain the quasi-steady state, in which the disturbance due to the initial effect is not significant. Since we established $T = 5.0$ s with $t = 20.0$ s in the previous work [30], the same combination will be used for NFTs in the next section. Then, by applying this time-averaging operation to the height and pressure, we introduce the following indices to evaluate the macroscopic attenuation effect:

$$\text{Depth reduction rate: } \frac{\overline{\Delta h}}{\overline{h_{\text{in}}}} \times 100 = \frac{\overline{h_{\text{out}}} - \overline{h_{\text{in}}}}{\overline{h_{\text{in}}}} \times 100 \quad [\%], \tag{16}$$

$$\text{Pressure loss: } \overline{\Delta P} = \overline{P}_{\text{out}} - \overline{P}_{\text{in}},$$

$$\left(\begin{aligned} P_{\text{out}} &= \frac{1}{|\partial \Omega_{\text{II}}|} \int_{\partial \Omega_{\text{II}}} P \, d\Omega \\ P_{\text{in}} &= \frac{1}{|\partial \Omega_{\text{I}}|} \int_{\partial \Omega_{\text{I}}} P \, d\Omega \end{aligned} \right), \tag{17}$$

where $\partial \Omega_{\text{I}}$ and $\partial \Omega_{\text{II}}$ are the surface domains, Surface-I and Surface-II, indicated in Fig. 2e, respectively. Here, $| \bullet |$ means the integrated value of $\bullet$, so that $\overline{P}_{\text{in}}$ and $\overline{P}_{\text{out}}$ are the spatiotemporal average of the pressure on Surface-I and Surface-II, and $\overline{h}_{\text{in}}$ and $\overline{h}_{\text{out}}$ are the time-averaged heights on Surface-I and Surface-II, respectively. It should be noted here that the regularized pressure loss in Eq. (17) is considered a key macroscopic factor in our previous multiscale evaluation of coastal forests [30].

Results

By conducting NFTs with several inflow depths and velocities, we can determine how the geometric modeling for trees influences the macroscopic or, equivalently, "homogenized", flow characteristics. After the combination of inflow depths and velocities to be considered is presented, the NFT results are discussed from the macro- and microscopic perspectives. More specifically, the macroscopic attenuation effect is evaluated using the indices defined in the previous section, and then the microscopic mechanisms that make a difference in macroscopic flow characteristics are clarified.

Numerical flow tests on arrayed cylinder/canopied-tree models

As a preliminary study, another series of NFTs have been performed on isolated canopied-tree and cylinder models (shown in Fig. 2a, b) at various combinations of inflow depths and velocities. The results are presented in Appendix A, from which it is found that there is no significant difference between the two models when only the trunk part is submerged. Therefore, the depth variations are limited to two cases: canopy submerged and fully submerged. On the other hand, the inflow speed is limited to $\hat{u}_1 = 0.30$ m s^{-1} or 0.55 m s^{-1}. If an actual tree is 10 times taller than the modeled trees (i.e., a natural tree standing $\mathcal{L} = 10L = 2.2$ m tall with $L = 0.22$ m), then the flow speed in a realistic situation is approximately $\mathcal{U} = 0.95$ m s^{-1} or 1.74 m s^{-1} according to Eq. (14). Thus, four cases

Table 2 Numerical flow test conditions for arrayed cylinder and canopied-tree models: initial flow speed $\hat{u}_1$ and depth $\hat{h}$

Case	Inflow speed $\hat{u}_1$ [m s^{-1}]	Inflow depth $\hat{h}$ [m]	$Fr = \hat{u}_1/\sqrt{g\hat{h}}$
A-1	0.30	0.15	0.25
A-2	0.50	0.15	0.41
B-1	0.30	0.25	0.19
B-2	0.50	0.25	0.32
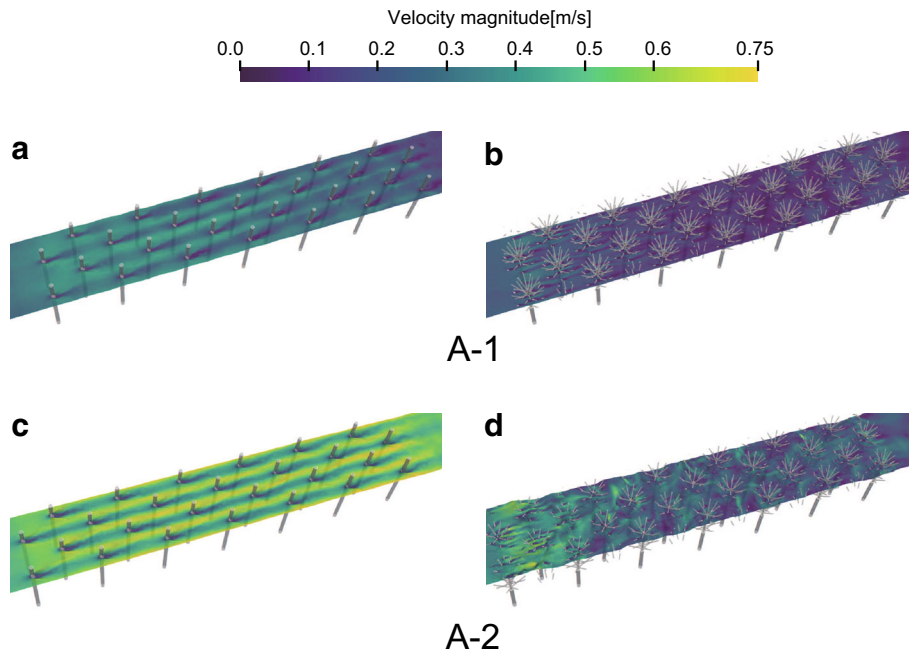
Fig. 3 Simulated free surface profiles at the final time step (top row: lower inflow speed with canopy submerged depth (A-1: $\hat{u}_1 = 0.300$ [m s^{-1}], $\hat{h} = 0.15$ [m]); bottom row: higher inflow speed with canopy submerged depth (A-2: $\hat{u}_1 = 0.55$ [m s^{-1}], $\hat{h} = 0.15$ [m])

with different inflow depths and velocities are considered for each of the canopied-tree and cylinder models; that is, we carried out eight NFTs in total. The inflow conditions to be considered in this section are summarized in Table 2. These conditions are regarded as "subcritical flow" and considered reasonable, as they were also employed in previous studies that examined the flow through vegetation; see, for example [16,44].

The simulated free surface profiles for two selected cases (A-1 and A-2) are provided in Fig. 3. These results show that the flow velocity is more attenuated in the cases with the canopied-tree model than in those with the cylinder model. Additionally, compared to the preliminary results from the isolated model in Appendix A, the arrayed setting appears to have greater velocity attenuation due to the crowd effect. Furthermore, the results with the cylinder model show a marked difference between fast and slow speeds; see Fig. 3a, c. However, in the results of the canopied-tree model, this tendency is not observed, and the complex geometry of the canopy and the adjacency of the trees seem to cause the low flow speed; see Fig. 3b, d. Additionally, a relatively intense disturbance is observed in the case of the canopied-tree model, as shown in Fig. 3d. Naturally, the deeper the depth is and the higher the inflow speed is, the more severe the disturbance.
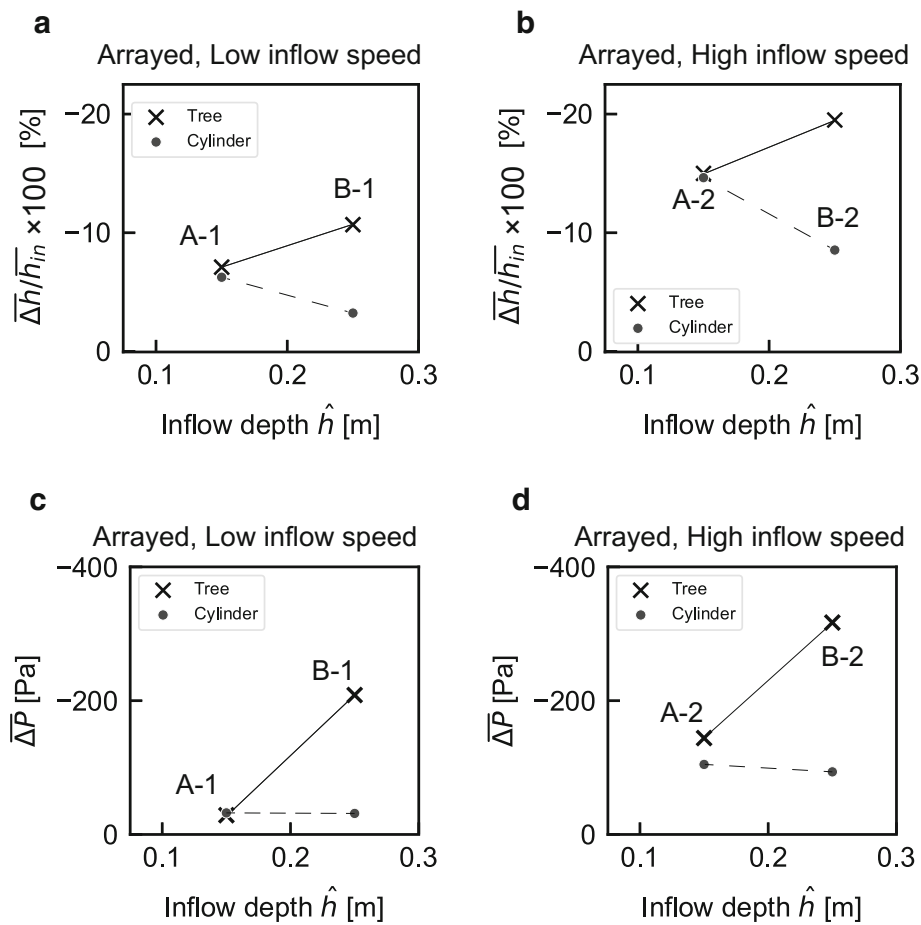
Fig. 4 Results of the macroscopic flow attenuation. **a**, **b** Depth reduction rate versus inflow depth (top row); **c**, **d** pressure loss values versus inflow depth (bottom row)

Macroscopic flow attenuation

Using the indices introduced in "Conversion of speed by Froude number", we discuss the flow attenuation properties from a macroscopic perspective.

Let us first focus on the depth reduction rate, defined as Eq. (16). Figure 4a, b show the dependency of the depth reduction rate on the inflow depth h. Notably, both h_{out} and h_{in} used in Eq. (16) are spatiotemporally averaged values evaluated on Surfaces-I and II that are indicated in Fig. 2e. As seen from these figures, the cases with fully submerged depths (B-1 and B-2) for the canopied-tree model are superior to those for the cylinder model in terms of depth attenuation performance. Indeed, the depth reduction in the cases of the canopied-tree models is 2.3–3.3 larger than that of the cylinder models. On the other hand, for the cases (A-1 and A-2) in which the canopy is partially submerged, the depth reduction rates are almost identical regardless of the difference in tree geometry.

The pressure losses calculated using Eq. (17) are shown in Fig. 4c, d and exhibit almost the same tendency as the depth reduction rates. That is, it is confirmed that the pressure losses in cases (B-1, B-2) with the canopied-tree model become larger than those of the cases for the cylinder model as the inflow depth is increased. When the canopy is partially submerged, a small inflow speed causes the two tree models to have almost the same pressure loss. Nevertheless, as seen from Fig. 4c, a higher inflow speed causes a difference
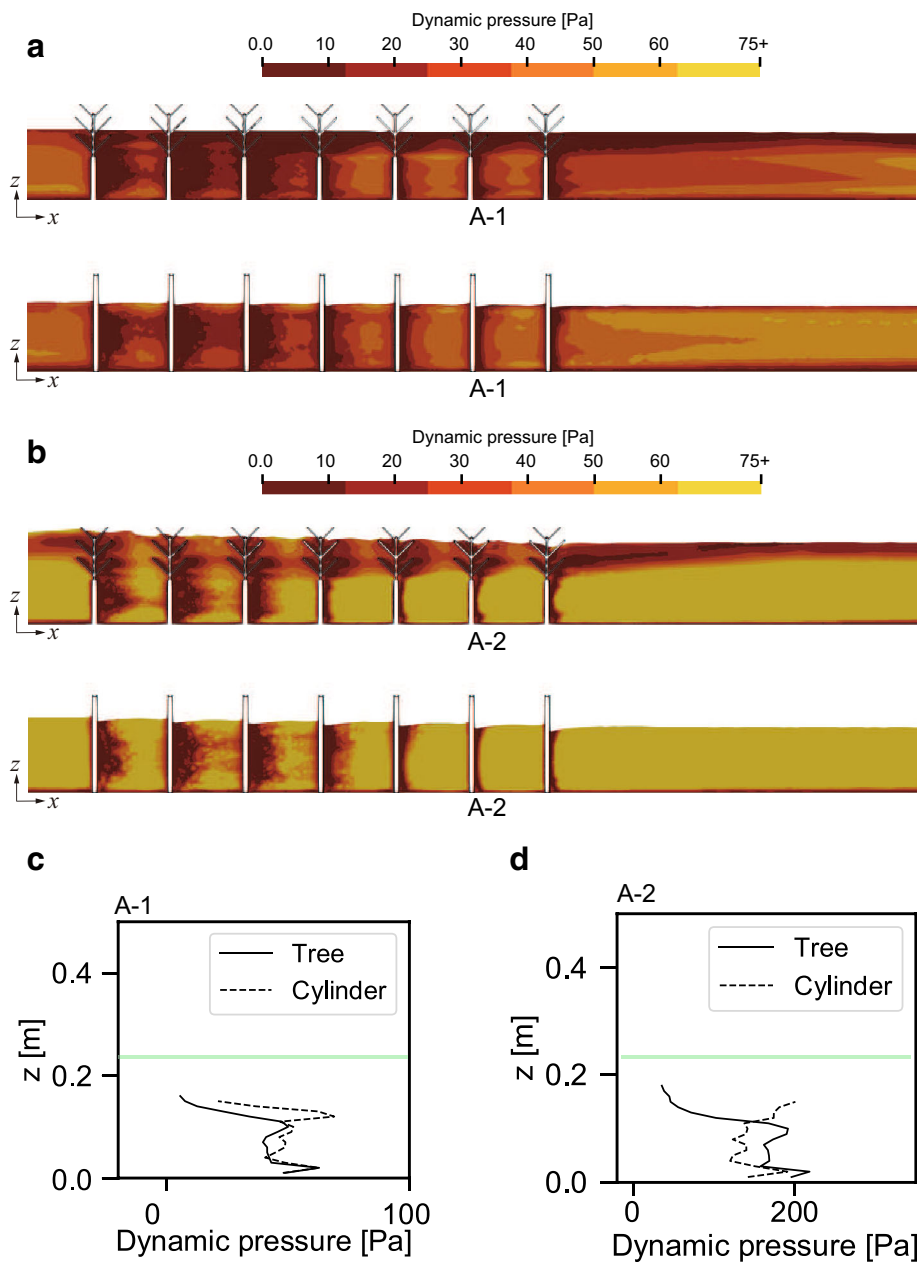
Fig. 5 Dynamic pressure distributions in canopy submerged depth inflow situations (A-1: $\hat{u}_1$=0.300 m s^{-1}, $\hat{h}$ = 0.15 m; A-2: $\hat{u}_1$=0.55 m s^{-1}, $\hat{h}$ = 0.15): **a**, **b** distributions on the $x - z$ surface at $y = 0.0$ and (**c**, **d**) vertical distributions behind the arrays, where the green line shows its top location (on Surface-II)

of approximately 40 [Pa] between the cases with the canopied-tree and cylinder models, even though the inflow depths are the same.

In summary, when using the canopied-tree model, the results of the cases in which the canopy is fully submerged exhibit approximately 3.4−6.6 times more severe macroscopic attenuation than the cases in which the canopy is partially submerged. This difference clearly occurs because the flow over the model is drastically attenuated because of the complex geometry of branches in the canopied-tree model. According to Nepf et al. [40], the effect is regarded as an additional bed roughness developed within the so-called
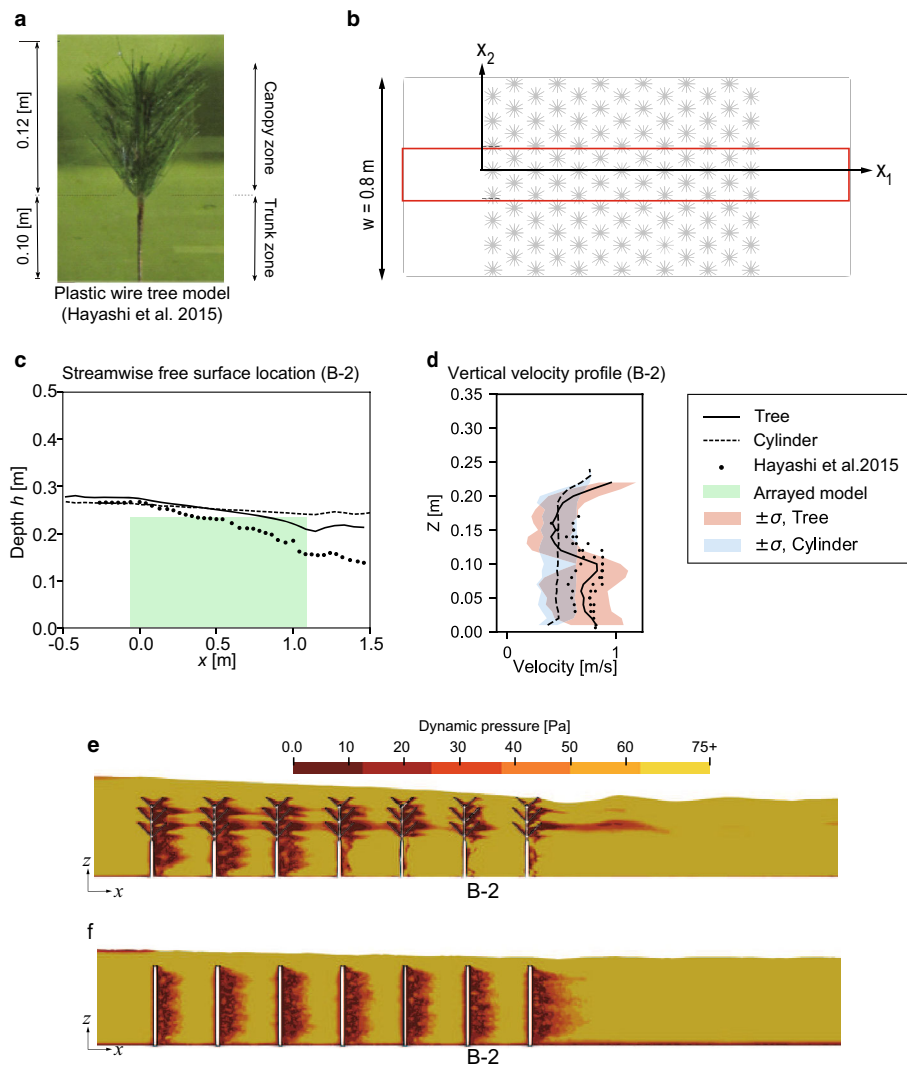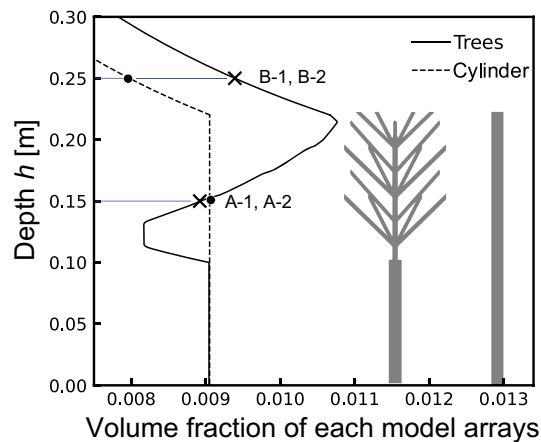
Fig. 6 Comparison with the hydraulic experiment performed by Hayashi et al. [39] with the plastic wire tree model shown in **a**. **b** The staggered arrangement of 97 miniature trees in the open channel used in the laboratory experiments by [39]. **c** The depth distribution in the streamwise directions, where the $\Delta h/h_{in}$ in Eq. (16) is 41.4% (Hayashi et al.), 26.8% (Tree) and 7.9% (Cylinder). The array of trees/cylinders is expressed with the green zone. **d** The spatiotemporally averaged velocity profile in the vertical direction on Surface-II. The standard deviations obtained from both canopied-tree models and cylinder models are expressed with red and blue bands. **e, f** compares the dynamic pressure distributions on the $x - z$ surface at $y = 0.0$

"roughness sublayer" that is formed above the canopy group. This is rephrased as a frictional effect of the group of canopied-trees on the macroscopic flow property.

Microscopic mechanism for macroscopic flow attenuation

To clarify the microscopic mechanism for the macroscopic flow attenuation effect discussed above, the flow within the LTD is investigated in more detail. As a measure to characterize the flow aspects at the microscopic level, we introduce the dynamic pressure as

$$\text{Dynamic pressure} = \frac{1}{2}\rho_f \, \boldsymbol{u} \cdot \boldsymbol{u}, \tag{18}$$

Nomura *et al. Advanced Modeling and Simulation in Engineering Sciences* (2023) 10:13

Page 13 of 25

Fig. 7 Volume fraction V_{model}/V_{all} of the array of both circular cylinder and the canopied-tree models depending on the submerged depth h

where $\boldsymbol{u}$ is the microscopic flow velocity obtained by NFTs. Figure 5a, b visualize the dynamic pressure distributions within the LTD. As seen from these figures, both the canopied-tree and cylinder models located upstream exhibit a large loss in dynamic pressure across the entire trunk, implying that the kinetic energy is severely dissipated. Additionally, these attenuation effects around the lower part of the trunk ($\hat{h} < 0.10$) tend to be weaker on the downstream side in both cases. In addition, the dynamic pressure is significantly reduced around the canopy of each canopied-tree model compared to that in the cylinder model. This is also verified from Fig. 9c, d in Appendix A, which show the distributions of the averaged dynamic pressure on Surface-ii when using the isolated model. Notably, as shown in Fig. 5a, b, this tendency is observed in all regions from upstream to downstream and is more noticeable in the cases with a higher flow speed. Additionally, the shear layers observed around the boundary between the stem and canopy are formed in the canopy tree models, while they are not in the cylinder models.

It is thus safe to conclude that the canopied-tree model with a detailed geometry of branches has a higher performance in reducing the dynamic pressure at the microscopic level than the circular cylinder model, and its attenuation effect is maintained in all regions from upstream to downstream. This effect must have been reflected in the depth reduction and pressure loss rates evaluated in the previous subsection, which characterize the macroscopic attenuation effect of the group of canopied-tree models.

It is worth mentioning that the absence of any turbulence models in our NFTs possibly leades to the underestimation of dynamic pressure losses. Though we have confirmed the validity of our NFTs by comparing them with the empirical drag force formulations, the attenuation due to the tree array, the so-called group effects, could possibly cause more intense dissipation due to the multiple wakes. Thus, the tree canopy possibly causes a greater pressure drop than that shown in Fig. 5a, b, since the turbulence around them is supposed to create energy dissipation. Therefore, the difference between the two models observed here cannot be overstated. This is because it affects the macroscopic attenuation, which is the final assessment that results from the microscopic observations.

Comparison with an actual hydraulic experiment

To justify the discussions above, the macroscopic attenuation behavior evaluated by the multiscale evaluation method is compared with that of the actual hydraulic experiment conducted by Hayashi et al. [39]. Figure 6a shows a miniature tree used in this laboratory experiment, which imitates a wild black pine tree and is made of plastic deformable wires. To mimic a coastal forest, ninety-seven miniature trees with almost the same geometry are arranged in a staggered manner in the water channel, whose upper view is shown in Fig. 6b. Meanwhile, our canopied-tree model, which is rigid (undeformable), was developed by reference to this miniature tree; indeed, the height and diameter of the trunk (or stem) and the length of the canopy mounted on the trunk are identical to each other. Additionally, the domain surrounded by the red-colored solid line shown in Fig. 6b corresponds to the LTD in our NFTs. Thus, we can discuss how the geometry modeling for NFTs affects the macroscopic flow characteristics in comparison with the experimental results.

We consider one of the test cases in the actual experiment, for which the flow condition is the same as in case B-2 in Table 2. Case B-2 has the most severe difference in macroscopic flow attenuation appeared between the cases with the canopied-tree and cylinder models in our NFTs, as shown in Fig. 4. Figure 6c shows the surface profiles obtained from the NFTs and experiment. Here, the solid and dashed lines are the results obtained by the canopied-tree and cylinder models, respectively, while the dotted line corresponds to the experimental ones. In order to discuss whether the cylinder model can be an alternative to the realistic trees as shown in Fig. 6a, the comparisons are provided for both the canopied-tree model vs. the experiment (plastic wire tree) and the cylinder model vs. the experiment (plastic wire tree). As seen from this figure, the simulated surface profiles with the canopied-tree model are closer to the experimental profiles than those of the cylinder model. From Eq. (16), the depth reduction rate in the laboratory experiment is calculated as 41.4%, which is approximately 1.5 times larger than that of the NFTs with the canopied-tree model ($\Delta h / h_{\text{in}} = 26.8\%$). Since the canopied-tree model is strictly rigid and its canopy part is quite different in geometry from that of the miniature tree, this level of discrepancy would be reasonable. On the other hand, the depth reduction rates ($\Delta h / h_{\text{in}} = 7.9\%$) for the case with the cylinder model are 5.2 times smaller than those of the experiment, which might not be negligible.

Figure 6d compares the velocity profiles in the vertical direction, which are spatiotemporally averaged values evaluated using Eq. (15) on Surface-II. The solid line in Fig. 6d showing the result with the canopied-tree model reproduces the disturbance of the flow around the canopy well. The red-colored band in this figure, which indicates the standard deviation of the time-averaged flow speed (solid line) on Surface-II, covers most of the flow speed profiles obtained in the laboratory experiment (dotted plots). However, the velocity profile obtained by the cylinder model, whose standard deviation is indicated with the blue-colored band, does not capture the characteristic feature of the experimental profile.

It is also confirmed from Fig. 6c, d that the NFT results using the canopied-tree model are satisfactory in terms of multiscale modeling of flow through coastal forest-like obstacles with complex geometry. Even though the NFTs were conducted in a part of the actual channel using the periodic boundary condition in the direction orthogonal to the overall flow, we could obtain surface and velocity profiles using the canopied-tree model that are comparable with those in the laboratory experiment. Notably, the flow speed behind

the canopy ($0.1 \leq z \leq 0.22$) is largely decreased compared to that behind the cylinder. Such tendencies are more obviously confirmed from the streamwise distribution of the pressure loss provided in Fig. 6e, f.

Nevertheless, as seen from the comparison with the experimental results, the NFT using the canopied-tree model underestimates the depth reduction rate. This discrepancy occurs because the flexibility, which would have serious influences on their resistance effect as reported by Manickathan et al. [45], is not considered in this study. The fact that the shape representation of canopies in the canopied-tree model is still coarse has also an impact. Furthermore, adding the turbulence model to our NFTs could contribute to improving the similarity with the hydraulic experiments. However, the accuracy of the present NFT method is acceptable enough to discuss the need for modeling a complex canopy geometry.

Discussion
Effect of detailed geometry on macroscopic flow characteristics
As discussed in the previous section, detailed tree modeling is worth performing for multiscale evaluation, especially in high inflow-speed and fully submerged depth situations. This insight was further confirmed by comparing the NFT results with those of the hydraulic experiment available in the literature [39].

For the case in which the canopy is fully submerged (B-2), the depth reductions in the NFT results with the canopied-tree and cylinder models differ by 0.048 [m], as shown in Fig. 4b ($\Delta h = -0.068$ m for the canopied-tree model; $\Delta h = -0.020$ m for the cylinder model). This means that the depth reduction performance would be underestimated by approximately 0.5 m at the real scale if we were to use the cylinder model with an identical height on the assumption that the real scale is ten times larger than the setup in the NFTs ($\lambda \cdot 0.048$ m with $\lambda = 10$). This difference must become larger if the trees have flexible bodies, as we confirmed in "Comparison with an actual hydraulic experiment". In fact, there is a 0.08 m difference in depth reduction between the laboratory experiment ($\Delta h = -0.10$ m) and the NFT with the cylinder model ($\Delta h = -0.02$ m). This corresponds to an error of at most a 0.8 m depth reduction at the real scale. Such differences could be minimized if the experiment employed a rigid miniature tree similar to the canopied-tree model used for the NFTs. Since the differences with the flexible trees is only 0.032 m ($\Delta h = -0.068$ m in NFT on the canopied-tree model; $\Delta h = -0.10$ m in experiments), the discrepancy can be diminished to 0.32 m. Additionally, as seen from Fig. 4d, the result of case B-2 recorded the largest pressure loss of 0.23 kPa among all the NFT results, which corresponds to an underestimation of 2.3 kPa at the real scale.

To explain why the canopied-tree and cylinder models provided quite different results, especially in the fully submerged depth cases, let us use the following volume fraction of trees as a quantitative indicator:

$$\text{Volume fraction} = \frac{V_{\text{model}}(h)}{V_{\text{all}}(h)}, \tag{19}$$

where V_{model} is the volume of the submerged portion of a tree model and V_{all} is the total volume excluding the air domain. Note here that V_{model} and V_{all} are functions of the vertical position, h, as

$$V_{\text{all}}(h) = |\delta Y_{\text{s}}^* \cup \delta Y_{\text{f}}|, \quad V_{\text{model}}(h) = |\delta Y_{\text{s}}^*|, \tag{20}$$

Nomura *et al. Advanced Modeling and Simulation in Engineering Sciences*(2023)10:13

Page 16 of 25

where $\delta Y_f \subset Y_f$ and $\delta Y_s^* \subset Y_s$ are the partial domains of fluid and trees inside the patched area of the staggered arrangement of trees in Fig. 2e (an equilateral triangle having edges of 0.1 m).

Accordingly, the volume fractions of the canopied-tree and cylinder models are calculated as shown in Fig. 7. The volume fractions differ greatly in the fully submerged depth cases (B-1 and B-2); in particular, the volume fraction of the canopied-tree model is much larger than that of the cylinder model. It is safe to deduce that this difference is reflected in the difference in depth reduction and pressure loss. On the other hand, as seen from this figure, the volume fractions of the two models are identical for the cases in which the canopy is partially submerged (Cases A-1 and A-2), although their upper geometries do not look similar. This is the reason why comparable depth reduction rates were obtained for these cases, as seen from Fig. 4.

The insight gained above further convinces us of the need for the 3D modeling of detailed tree geometry while raising an alarm for the use of conventional 2D modeling, such as the projection area, which is an index often used in the drag force modeling in conjunction with the drag coefficients. In fact, in the preliminary studies carried out with the isolated canopied-tree model, we found that the discrepancy arises in the drag force evaluations if we take the detailed geometry into account by just the 2D projected area. Considering that correspondences are observed with the cylindrical models based on empirical drag coefficients, the validity of our assertion is reasonable. Thus, whether the detailed geometry must be modeled should be evaluated based on 3D information, such as the ratio of the submerged volume. For further support of this argument, please refer Fig. 10 in Appendix A.

Flow situations requiring detailed geometry in multiscale evaluations

Based on the findings of this study, we further explore the flow situations requiring detailed geometric modeling for trees in the multiscale evaluation of coastal forests in a more general context.

First, we observed that the effect of the geometry of the canopied-tree model on the macroscopic attenuation property is much greater than that of the cylinder model when a large part of the canopy geometry is submerged with a relatively high flow speed. Although we have imposed "subcritical flow" conditions for our NFTs in the LTD, flow states in reality possibly become critical/supercritical flow states (Fr $\geq$ 1.0) [46], for which the impact of the difference in geometry on the macroscopic flow characteristics evaluated by the multiscale evaluation method would become greater.

Second, our simulation results reveal a macroscopically comparable attenuation effect between the cases with the canopied-tree and cylinder models when they are not fully submerged. However, even in such a case, we do not wish to actively encourage the use of the cylinder model in the modeling of a coastal forest. In this submerged level, the geometries of the submerged portion of both models are seemingly different, but their volume fractions are comparable, as we demonstrated in Fig. 7. Therefore, we cannot apply binary criteria such as "detailed geometries should be modeled if they are submerged" or "detailed geometries are not required if they are not submerged". To clarify the criteria when the two models significantly diverge, further research is warranted with 3D information about the detailed geometries and is left to future work.

Nomura *et al. Advanced Modeling and Simulation in Engineering Sciences*(2023)10:13

Page 17 of 25

Third, the above-gained insight suggests that specific tree species might always require detailed modeling of their complicated geometries. For instance, some species of mangrove trees (e.g., *Rhizophora* studied by Jaisankar [47]) have a complex root system, namely, the so-called prop root system. In fact, Zhang et al. [48] reported that the complex secondary flow and blockage effects were caused by the complex prop root system of mangroves. Of course, a simple comparison between the effect of branches in our canopied-tree model and the root system might not be appropriate, as the vertical positions of their complex geometries differ. Nevertheless, such a difference in the vertical location of the complex geometry does not exclude our suggestion because they are similar in terms of geometrical complexity. Additionally, the consideration of a tree's detailed geometries would be mandatory for multiscale evaluation if the crown-like morphology occupies most of the submerged volume of a tree, such as shrubs or bushes.

Moreover, as mentioned at the beginning of "Numerical flow tests on arrayed cylinder/canopied-tree models" with reference to Appendix A, simple cylinder models are sufficient if the flow depth is expected to be below the canopy height. This situation is applicable when the tree species are tall, for example, black pine trees, in which the canopy zone is located very high above ground level once they are sufficiently mature. This insight is consistent with the simulation done by Ohira et al. [49], who argued that a high canopy had a low contribution to the macroscopic attenuation effect.

Conclusion

In this paper, we have investigated the influence of detailed geometric modeling of trees on their macroscopic attenuation effect against tsunami-like flow by applying the multiscale evaluation method previously developed by the authors [30]. The main component of the multiscale evaluation method is numerical flow tests (NFTs), which are realized by carrying out 3D flow simulations in a local test domain (LTD). The LTD was assumed to be the representative elementary volume (REV) to characterize the macroscopic flow behavior, in which the canopied-tree and cylinder models were arranged in a staggered manner. After the corresponding governing equations with analysis conditions were presented, we introduced two indices, depth reduction rate and pressure loss, for evaluating the macroscopic flow characteristics relevant to the multiscale evaluation. Then, a series of NFTs were conducted under various inflow conditions with different inflow velocities and depths to evaluate the macroscopic attenuation property represented by the indices and discuss the effect of canopies on the tree model.

From the results of NFTs, we discussed the flow situations requiring the detailed tree geometry in a general context and reported the following findings:

- The flow situation where the depth exceeds the canopy height or, equivalently, where the detailed geometry of trees occupies a large portion of the submerged depth, requires a detailed geometry for multiscale evaluation.
- Nonbinary criteria should be employed whether the modeling of the detailed geometry is encouraged or not.
- Specific tree species, such as mangroves, always necessitate information about their detailed geometries, and vice versa.

The above insights suggest the answer to the question we posed in the Introduction in view of the conventional ambiguous standards; that is, in what situation do we need to model coastal forest by an array of trees with complex tree geometries instead of simple vertical cylinders, or vice versa? The findings are seemingly intuitive and trivial but directly linked to the key to the solution. Therefore, it is doubtless that the results of this study will help disseminate natural trees as Eco-DRR measures in the future by improving the method of multiscale evaluation to reliably assess their performance.

Further investigation into the geometric effect on the macroscopic flow characteristics would fortify the suggestion in this study. In particular, our argument that information about 3D volume occupancy for vegetation is needed in addition to 2D information must be scrutinized by NFTs with various canopied-tree models with more complex geometry. With this information, the criteria for the geometric information would be established as a function of the submerged depth, inflow speed, 3D volume occupancy rate and other conventional parameters. Once these parameters have been realized, the established criteria could be applied in the NFTs to reasonably evaluate the macroscopic attenuation property that can be used in the practical 2D simulations. For that purpose, we must pursue more realistic 3D tree shape generations, more advanced fluid–structure interaction schemes, and turbulence models for NFTs with a tree model with flexible branches. In addition to the insights into the geometric effects of the trees, discussions on the LTD, in terms of the scale, the streamwise length, domain shape (e.g., cubic domain), or the periodic boundary conditions, are also effective to make the framework more accessible.

Appendix A: Preliminary study with isolated canopied-tree and cylinder models

To effectively carry out the NFTs on the arrayed model with limited cases, we need to roughly grasp the effect of the detailed geometry of the canopy on the flow characteristics. For that purpose, we conduct a preliminary study by conducting numerical flow simulations with the isolated canopied-tree and cylinder models.

A.1 Model setup and conditions for numerical flow tests

Figure 8a, b show the isolated single canopied-tree and cylinder model equipped in the LTD. Each model is located at (x, y) = (0.52, 0.0) [m] in an LTD that has the same size as in "Numerical flow tests for identifying flow conditions requiring detailed geometric modeling". As test surfaces, Surface-i and Surface-ii are placed in front of and behind the model in the LTD with a width of Δw (= 0.20) [m], as shown in Fig. 8c. It should be noted that the LTD of this setting is not eligible for an REV, as it does not contain a sufficient number of vertical structures (either canopied-tree or cylinder models).

The equations governing the flow motion for NFTs are identical to those in "Governing equations for NFTs in the LTD". In addition, the boundary and initial conditions are the same as before, except for the following slip-type boundary conditions imposed on both sidewalls:

$$u_y\big|_{\partial Y_{-2}} = u_y\big|_{\partial Y_{+2}} = 0, \tag{21}$$

along with the traction-free conditions in the x and z-directions. The information about the 3D flow simulations for NFTs is summarized in Table 3.
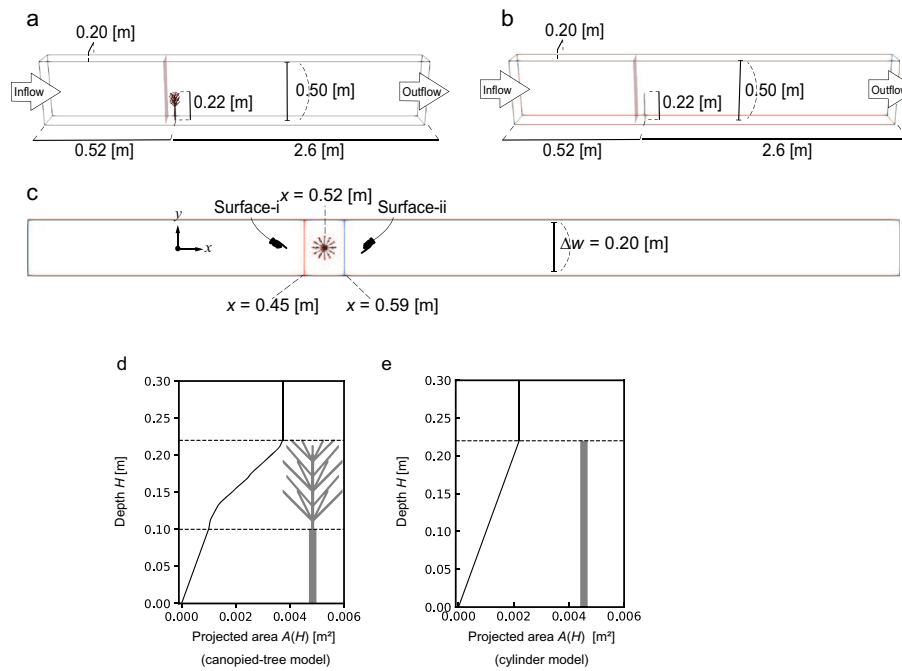
Fig. 8 Setup of the NFTs on the canopied-tree/cylinder model: **a**, **b** LTDs accommodating both isolated models and (**c**) top views of the isolated canopied tree models in the LTD. **d**, **e** Projected areas $A(H)$s of each model

Table 3 Information about 3D flow simulations in preliminary study

Model type	Tree	Cylinder
Nodes	175,411	122,867
Elements	896,039	625,471
Element size : πd	1:40	
Time step Δt	0.001 [s]	
Data sampling	100 [Hz] (Per 0.01 [s])	
Density ρ	998 [kg/m^3]	
Viscosity μ	1.01e−3 [Pas]	

Table 4 Numerical flow test conditions for an isolated cylinder model and a canopied-tree model: initial flow speed $\hat{u}_1$ and depth $\hat{h}$

Case	Inflow speed $\hat{u}_1$ (m s^{-1})	Inflow depth $\hat{h}$ (m)	Fr $= \hat{u}_1/\sqrt{g\hat{h}}$
a-1	0.30	0.05	0.43
a-2	0.55	0.05	0.79
b-1	0.30	0.10	0.30
b-2	0.55	0.10	0.56
c-1	0.30	0.15	0.25
c-2	0.55	0.15	0.45
d-1	0.30	0.25	0.19
d-2	0.55	0.25	0.35

Nomura *et al. Advanced Modeling and Simulation in Engineering Sciences* (2023) 10:13

Page 20 of 25

Considering the difference in the geometries of the models, we establish several inflow depth conditions: a trunk submerged depth ($\hat{h} \leq 0.10$), a canopy submerged depth ($0.10 < \hat{h} \leq 0.22$), and a fully submerged depth ($0.22 < \hat{h}$). Additionally, the inflow speed is also controlled at $\hat{u}_1 = 0.300 \,[\mathrm{m\,s^{-1}}]$ and $0.55 \,[\mathrm{m\,s^{-1}}]$. These flow conditions employed in this appendix are summarized in Table 4. Here, the Froude numbers (Fr) have been calculated with the inflow depth $\hat{h}$ as the representative length L. Fr < 1 is recognized for all cases.

A.2 Flow characteristics evaluated from a local perspective

We characterize the flow through the isolated model from a local perspective. Figure 9 shows the distributions of the dynamic pressure (defined by Eq. (18)) for cases d-1 and d-2 at the final step (t=20.0 [s]). As seen from these figures, the wake behind the canopied-tree model is more intense than that of the cylinder model; i.e., both the width and the length of the wake are much broader and more prolonged in the downstream direction. This tendency is more noticeable for the cases with higher speed, as seen in Fig. 9b. To further investigate the flow characteristics at the local level, the distributions of the dynamic pressure behind each mode along the vertical line on Surface-ii ($(x, y) = (0.59, 0.0)$) are provided in Fig. 9c, d. It can be confirmed from the figure that the pressure loss behind the canopied-tree model is much greater than that behind the circular cylinder model. Such a flow attenuation effect is further strengthened when many vertical obstacles are placed, as in the REV in this study, which follows the previous study [30]—this is the so-called group effect.

A.3 Flow characteristics evaluated from a global perspective

A.3.1 Measure of fluid force

To evaluate the fluid forces from a global perspective, we introduce two measures. One is the exerted force on the model defined as

$$f = \int_{\partial Y_s^*} \boldsymbol{t} \cdot \boldsymbol{n} \, d\Omega \ \ \text{where} \ \ \boldsymbol{t} = \boldsymbol{\sigma}_{\mathrm{f}} \cdot \boldsymbol{n} \ [\mathrm{Pa}], \tag{22}$$

which can be calculated by taking the sum of the nodal forces, namely, the net force. The other is the conventional or empirical definition of drag force using both the spatiotemporal averaged flow velocity and depth (mean fluid depth hereafter), U and H, and is written as

$$\text{Drag force} = \frac{1}{2} \rho C_D A(H) U^2 \ [\mathrm{N}], \tag{23}$$

where $\boldsymbol{\sigma}_{\mathrm{f}}$ is the stress tensor and $\boldsymbol{n}$ is an outward unit vector normal to the surface ∂Y_s^*. Here, C_D is the drag coefficient, and $A(H)$ is the total frontal area of the model on the $y - z$ plane. Additionally, U and H are defined as

$$U = \frac{1}{|\Omega_i|} \int_{\Omega_i} u_x(\hat{x}, y, z) \, d\Omega, \ \text{and} \ H = \frac{1}{|\Gamma_i|} \int_{\Gamma_i} h(\hat{x}, y) \, dy, \tag{24}$$

where $u_x(\hat{x}, y, z)$ and $h(\hat{x}, y)$ are the x-component of flow velocity and flow depth obtained on Surface-i (placed at $\hat{x} = 0.45$ [m]) as solutions of the 3D flow simulation. Additionally, Ω_i and $|\Omega_i|$ are the partial domain of Surface-i submerged in the fluid and its area, respectively, both of which vary with the mean flow depth H. Additionally, Γ_i and $|\Gamma_i| = \Delta w$ are the fluid surface domain of Ω_i and its length, respectively.
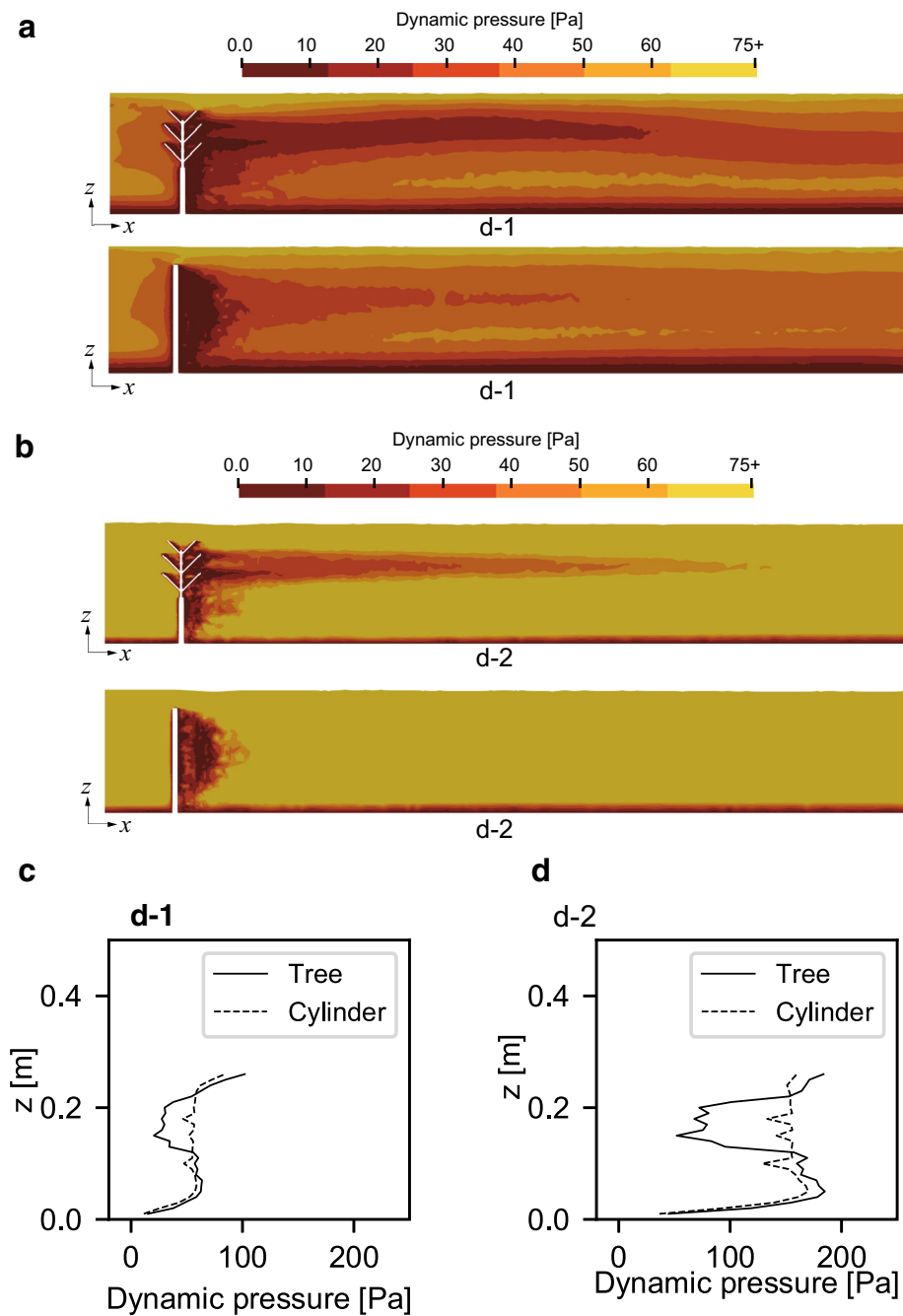
Fig. 9 Dynamic pressure distributions in fully submerged depth inflow situations (d-1: $\hat{u}_1 = 0.300$ [m s^{-1}], $\hat{h} = 0.25$ [m], d-2: $\hat{u}_1 = 0.55$ [m s^{-1}], $\hat{h} = 0.25$ [m]): **a**, **b** Distributions on the $x - z$ surface at $y = 0.0$. **c**, **d** Vertical distributions behind the arrays on Surface-II

The drag coefficient C_D can be estimated in relation to the Reynolds number Re, which is identified in this setting as

$$\text{Re} = \frac{\rho U d'}{\mu}, \text{ where } d' = \frac{A(H)}{H}. \tag{25}$$

According to this definition, the Reynolds numbers corresponding to the flow speeds provided in Table 4 range from 2990 to 4825. Then, using the diagram provided in Weisstein

Table 5 Time-averaged values of force f as a solution of the NFTs

Case	Mean force $\bar{f}$ [N]	
No.	Tree	Cylinder
a-1	0.02	0.02
a-2	0.05	0.05
b-1	0.04	0.05
b-2	0.11	0.11
c-1	0.08	0.05
c-2	0.26	0.17
d-1	0.17	0.07
d-2	0.54	0.25
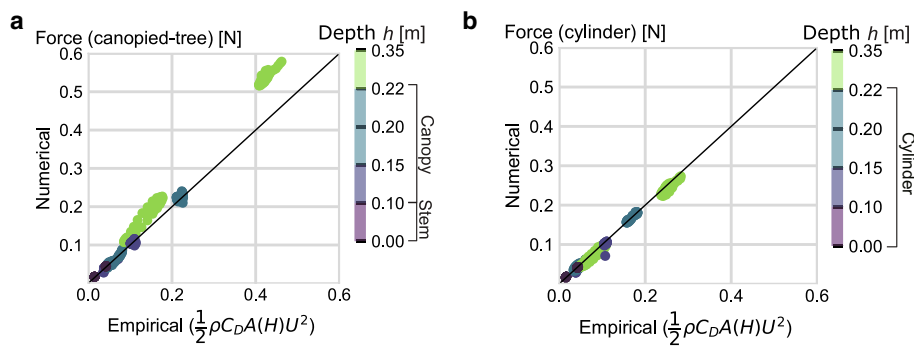
Fig. 10 Relationship between the numerically measured net force $\bar{f}$ and conventional drag force, **a** Canopied-tree model; **b** Cylinder model

[50], the average value of the drag coefficient is approximately $C_D = 0.88$ for both the canopied-tree and cylinder models. Additionally, the dependencies of $A(H)$ on the mean flow depth H are illustrated for both models in Fig. 8d, e.

A.3.2. Difference in flow characteristics

The forces evaluated by (22) are averaged in time using Eq. (15) ($t = 15.0$, $T = 5.0$) and summarized in Table 5. As seen from these values, an apparent difference between the canopied-tree and cylinder models is recognized when the canopy is submerged. The forces calculated for the canopied-tree model with submerged or fully submerged depths (c-1/c-2 or d-1/d-2, respectively) are approximately two times higher than those for the cylinder model. On the other hand, in the cases where a trunk is submerged, the values obtained for both models are almost identical.

Figure 10 shows the relationships between the net force exerted on the models calculated using Eq. (22) and the drag force calculated using (23) every 0.1 sec during the time interval $t = [15.0, 20.0]$. Here, the color of the markers indicates the mean flow depth H in Eq. (24)$_2$. As seen from Fig. 10b, the force acting on the cylinder model coincides with the conventional force measure for all the depth cases. A similar tendency can be seen from the results obtained for the canopied-tree model in Fig. 10a. However, the green markers, which correspond to the cases in which the models are fully submerged, deviate from the line indicating that both values are the same, implying that the conventional measure is erroneous for the canopied-tree model.

A.4 Summary of the preliminary study

The results of the preliminary study are summarized as follows:

- There is no significant difference between the two models when only the trunk is submerged.
- The difference in flow attenuation between the two models becomes larger if a larger portion of the canopy is submerged.
- If a large portion of the canopy is submerged, the difference in flow attenuation between the two models becomes larger, and the conventional drag force calculation can give erroneous results.
- The fully submerged situation calls for the careful consideration of not only conventional information, such as the 2D projected area $A(H)$, but also other factors representing the information about the 3D detailed geometry.

Abbreviations

LTD	Local test domain
REV	Representative elementary volume
FEM	Finite element method
NFT(s)	Numerical flow test(s)

Availability of data and materials
The data that support the findings of this study are available from the corresponding author, R. Nomura, upon reasonable request.

Declarations

Competing interests
The authors declare that they have no competing interests.

References
1. Nehren U, Sudmeier-Rieux K, Sandholz S, Estrella M, Lomarda M, Guillén T. The ecosystem-based disaster risk reduction case study and exercise source book. CNRD/PEDRR. 2014;24.
2. UNISDR: Sendai Framework for Disaster Risk Reduction 2015–2030. https://www.wcdrr.org/preparatory/post2015.html; 2015.
3. Shuto N. The effectiveness and limit of tsunami control forests. Coastal Eng Jpn. 1987;30(1):143–53.
4. Danielsen F, Sørensen MK, Olwig MF, Selvam V, Parish F, Burgess ND, Hiraishi T, Karunagaran VM, Rasmussen MS, Hansen LB, et al. The Asian tsunami: a protective role for coastal vegetation. Science. 2005;310(5748):643–643.
5. Harada K, Imamura F. Effects of coastal forest on tsunami hazard mitigation—a preliminary investigation. In: Tsunamis. 1st ed. Dordrecht: Springer; 2005. p. 279–92.
6. Takayama T, Katoh K, Imamura F, Kawata Y, Murata S, Takahashi S. Tsunami: to Survive from Tsunami. 2nd ed. Singapore: World Scientific; 2018.
7. Tanaka N, Yasuda S, Iimura K, Yagisawa J. Combined effects of coastal forest and sea embankment on reducing the washout region of houses in the great east japan tsunami. J Hydro-Environ Res. 2014;8(3):270–80.

Nomura *et al. Advanced Modeling and Simulation in Engineering Sciences* (2023)10:13

Page 24 of 25

8. Strusińska-Correia A. Tsunami mitigation in Japan after the 2011 tōhoku tsunami. Int J Disaster Risk Reduct. 2017;22:397–411.

9. Pasha GA, Tanaka N, Yagisawa J, Achmad FN. Tsunami mitigation by combination of coastal vegetation and a backward-facing step. Coast Eng J. 2018;60(1):104–25.

10. Nepf HM. Drag, turbulence, and diffusion in flow through emergent vegetation. Water Resour Res. 1999;35(2):479–89.

11. Neary VS. Numerical solution of fully developed flow with vegetative resistance. J Eng Mech. 2003;129(5):558–63.

12. Iimura K, Tanaka N. Numerical simulation estimating effects of tree density distribution in coastal forest on tsunami mitigation. Ocean Eng. 2012;54:223–32.

13. Irish JL, Weiss R, Yang Y, Song YK, Zainali A, Marivela-Colmenarejo R. Laboratory experiments of tsunami run-up and withdrawal in patchy coastal forest on a steep beach. Nat Hazards. 2014;74(3):1933–49.

14. Mei CC, Chan I-C, Liu PL-F. Waves of intermediate length through an array of vertical cylinders. Environ Fluid Mech. 2014;14(1):235–61.

15. Maza M, Lara JL, Losada IJ. Tsunami wave interaction with mangrove forests: a 3-d numerical approach. Coast Eng. 2015;98:33–54.

16. Anjum N, Tanaka N. Experimental study on flow analysis and energy loss around discontinued vertically layered vegetation. Environ Fluid Mech. 2019;1–27.

17. Tanaka N, Sasaki Y, Mowjood M, Jinadasa K, Homchuen S. Coastal vegetation structures and their functions in tsunami protection: experience of the recent Indian Ocean tsunami. Landscape Ecol Eng. 2007;3(1):33–45.

18. Tanaka N. Vegetation bioshields for tsunami mitigation: review of effectiveness, limitations, construction, and sustainable management. Landscape Ecol Eng. 2009;5(1):71–9.

19. Tanaka N, Takenaka H, Yagisawa J, Morinaga T. Estimation of drag coefficient of a real tree considering the vertical stand structure of trunk, branches, and leaves. Int J River Basin Manage. 2011;9(3–4):221–30.

20. Maza M, Adler K, Ramos D, Garcia AM, Nepf H. Velocity and drag evolution from the leading edge of a model mangrove forest. J Geophys Res Oceans. 2017;122(11):9144–59.

21. Suzuki T, Hu Z, Kumada K, Phan LK, Zijlema M. Non-hydrostatic modeling of drag, inertia and porous effects in wave propagation over dense vegetation fields. Coast Eng. 2019;149:49–64.

22. Strusińska-Correia A, Husrin S, Oumeraci H. Tsunami damping by mangrove forest: a laboratory study using parameterized trees. Nat Hazard. 2013;13(2):483–503. https://doi.org/10.5194/nhess-13-483-2013.

23. Ohira W, Honda K, Nagai M, Ratanasuwan A. Mangrove stilt root morphology modeling for estimating hydraulic drag in tsunami inundation simulation. Trees. 2013;27(1):141–8.

24. Chang C-W, Mori N, Tsuruta N, Suzuki K. Estimation of wave force coefficients on mangrove models. J Jpn Soc Civil Eng Ser B2 Coast Eng. 2019;75(2):1105–10.

25. Chang C-W, Mori N. Application of Boussinesq modeling on water waves through mangroves. J Jpn Soc Civil Eng Ser B2 (Coast Eng). 2020;76(2):49–54.

26. Shlyakhter I, Rozenoer M, Dorsey J, Teller S. Reconstructing 3d tree models from instrumented photographs. IEEE Comput Graphics Appl. 2001;21(3):53–61.

27. Sun R, Jia J, Jaeger M. Intelligent tree modeling based on l-system. In: 2009 IEEE 10th International Conference on Computer-Aided Industrial Design & Conceptual Design. 2009; pp. 1096–1100. IEEE.

28. Paynter I, Saenz E, Genest D, Peri F, Erb A, Li Z, Wiggin K, Muir J, Raumonen P, Schaaf ES, et al. Observing ecosystems with lightweight, rapid-scanning terrestrial lidar scanners. Remote Sens Ecol Conserv. 2016;2(4):174–89.

29. Prusinkiewicz P, Lindenmayer A. The algorithmic beauty of plants. New York: Springer; 2012.

30. Nomura R, Takase S, Moriguchi S, Terada K, LeVeque RJ. Multiscale evaluation method of the drag effect on shallow water flow through coastal forests based on 3d numerical simulations. Int J Numer Methods Fluids. 2021.

31. Bear J. Dynamics of fluids in porous media. Massachusetts: Courier Corporation; 2013.

32. Brooks AN, Hughes TJR. Streamline upwind/petrov-galerkin formulations for convection dominated flows with particular emphasis on the incompressible navier-stokes equations. Comput Methods Appl Mech Eng. 1982;32(1–3):199–259.

33. Tezduyar TE. Stabilized finite element formulations for incompressible flow computations. 1991;28:1–44.

34. Chiu P-H, Lin Y-T. A conservative phase field method for solving incompressible two-phase flows. J Comput Phys. 2011;230(1):185–204.

35. Takada N, Matsumoto J, Matsumoto S. Phase-field model-based simulation of motions of a two-phase fluid on solid surface. J Comput Sci Technol. 2013;7(2):322–37.

36. Sanchez-Palencia E. Non-Homogeneous media and vibration theory. Berlin: Springer; 1980. https://doi.org/10.1007/3-540-10000-8.

37. Terada K, Ito T, Kikuchi N. Characterization of the mechanical behaviors of solid-fluid mixture by the homogenization method. Comput Methods Appl Mech Eng. 1998;153(3):223–57. https://doi.org/10.1016/S0045-7825(97)00071-6.

38. Geers MGD, Kouznetsova VG, Matouš K, Yvonnet J. (eds.) Homogenization Methods and Multiscale Modeling: Nonlinear Problems, pp. 1–34. Wiley, Hoboken; 2017

39. Hayashi K, Tada T, Shigihara Y. Fluid forces and hydraulic resistance of trees in river. In: 18th Applied Mechanics Symposium, Kanazawa, Japan. 2015; pp. 291–292

40. Nepf H, White B, Lightbody A, Ghisalberti M. Transport in aquatic canopies. In: Gayev, Y.A., C.R. Hunt, J, editors. Flow and Transport Processes with Complex Obstructions, 1st edn. NATO Science Series II: Mathematics, Physics and Chemistry. 2007; vol. 236, pp. 221–250. Springer, Kyiv, Ukraine. Chap. 6.

41. Takase S, Moriguchi S, Terada K, Kato J, Kyoya T, Kashiyama K, Kotani T. 2d–3d hybrid stabilized finite element method for tsunami runup simulations. Comput Mech. 2016;58(3):411–22.

42. Orlanski I, et al. A simple boundary condition for unbounded hyperbolic flows. J Comput Phys. 1976;21(3):251–69.

43. Yoshida T, Watanabe T. Sommerfeld radiation condition for incompressible viscous flows. In: V European Conference on Computational Fluid Dynamics (ECCOMAS CFD 2010), Lisbona. 2010.

44. Pasha GA, Tanaka N. Undular hydraulic jump formation and energy loss in a flow through emergent vegetation of varying thickness and density. Ocean Eng. 2017;141:308–25.

Nomura *et al. Advanced Modeling and Simulation in Engineering Sciences*(2023)10:13

Page 25 of 25

45. Manickathan L, Defraeye T, Allegrini J, Derome D, Carmeliet J. Comparative study of flow field and drag coefficient of model and small natural trees in a wind tunnel. Urban Forest Urban Green. 2018;35:230–9.

46. Iwai S, Goto K. Threshold flow depths to move large boulders by the 2011 Tohoku-Oki tsunami. Sci Rep. 2021;11(1):1–10.

47. Jaisankar I, Velmurugan A, Swarnam TP. Chapter 24–bioshield: an answer to climate change impact and natural calamities? In: Sivaperuman C, Velmurugan A, Singh AK, Jaisankar I, editors. Biodiversity and climate change adaptation in tropical islands. 1st ed. Port Blair: Academic Press; 2018. p. 667–98. https://doi.org/10.1016/B978-0-12-813064-3.00024-7.

48. Zhang X, Chua VP, Cheong H-F. Hydrodynamics in mangrove prop roots and their physical properties. J Hydro-Environ Res. 2015;9(2):281–94.

49. Ohira W, Honda K, Harada K. Reduction of tsunami inundation by coastal forests in Yogyakarta, Indonesia: a numerical study. Nat Hazard. 2012;12(1):85–95.

50. Weisstein EW. Cylinder Drag. https://scienceworld.wolfram.com/physics/CylinderDrag.html. 2007; Online; Accessed 1 Feb 2021.

Publisher's Note